Eight-channel transceiver RF coil array tailored for (1)H/(19)F MR of the human knee and fluorinated drugs at 7.0 T.

Ji, Y., Waiczies, H., Winter, L., Neumanova, P., Hofmann, D., Rieger, J., Mekle, R., Waiczies, S., Niendorf, T.

NMR in Biomedicine
2015 JUN ; 28(6): 726-737
Version of record online: 2015 APR 27
doi: 10.1002/nbm.3300
Publisher: Wiley-Blackwell

Eight Channel Transceiver Radiofrequency Coil Array Tailored for $^{1}H/^{19}F$ Magnetic Resonance of the Human Knee and Fluorinated Drugs at 7.0 Tesla

Yiyi Ji [1,2,§], Helmar Waiczies [1,3,§], Lukas Winter [1], Pavla Neumanova [1], Daniela Hofmann [1], Jan Rieger [3], Ralf Mekle [4], Sonia Waiczies [1], Thoralf Niendorf [1,5]

[1] Berlin Ultrahigh Field Facility (B.U.F.F.), Max Delbrück Center for Molecular Medicine, Berlin, Germany

[2] Institute of Biophysics and Biomedical Engineering, Faculty of Sciences of the University of Lisbon, Lisbon, Portugal

[3] MRI.TOOLS GmbH, Berlin, Germany

[4] Medical Physics, Physikalisch-Technische Bundesanstalt, Berlin, Germany

[5] Experimental and Clinical Research Center, a joint cooperation between the Charité Medical Faculty and the Max Delbrück Center for Molecular Medicine, Berlin, Germany.

[§] Equally contributing authors

Correspondence:

Prof. Dr. Thoralf Niendorf, Ph.D.

Max Delbrück Center for Molecular Medicine

Robert Roessle Strasse 10

13125 Berlin, Germany

phone: +49 30 9406 4505

e-mail: thoralf.niendorf@mdc-berlin.de

Word account: 5637

Short title: $^{1}H/^{19}F$ Magnetic Resonance of the Human Knee and Fluorinated Drugs at 7.0 Tesla

Key words: magnetic resonance, MRI, fluorine magnetic resonance, ultrahigh field MRI, radiofrequency coil, non-steroidal anti-inflammatory drug, drug monitoring

List of Abbreviations

^{19}F MR	fluorine magnetic resonance
ABS	acrylonitrile butadiene styrene
B_0	static magnetic field strength
B_1^+	transmission field
CAD	computer aided design
CNC	computer numerical control
DC	dendritic cell
EMF	electromagnetic field
f	frequency in Hertz
FA	flufenamic acid
FDTD	finite-difference time-domain
GRE	gradient echo
IEC	international electrical commission
NSAID	non-steroidal anti-inflammatory drug
PCB	printed circuit board
PTFE	polytetrafluoroethylene
RF	radiofrequency
ROI	region of interest
SAR	specific absorption rate
SNR	signal-to-noise ratio
S-parameter	scattering parameter
SPECIAL	Spin Echo full Intensity Acquired Localized
SVS	single voxel spectroscopy
T_1	longitudinal relaxation time
T_2	transversal relaxation time
TE	echo time
TR	repetition time
Tx/Rx	transmit/receive
UHF-MR	ultrahigh field magnetic resonance

Graphical abstract

Eight Channel Transceiver Radiofrequency Coil Array Tailored for $^{1}H/^{19}F$ Magnetic Resonance of the Human Knee and Fluorinated Drugs at 7.0 Tesla

Yiyi Ji [1,2,§], Helmar Waiczies [1,3,§], Lukas Winter [1], Pavla Neumanova [1], Daniela Hofmann [1], Jan Rieger [1,3], Ralf Mekle [4], Sonia Waiczies [1], Thoralf Niendorf [1,5]

Short summary

This work demonstrates the feasibility of an eight-channel dual-tuned transceiver surface radiofrequency (RF) coil array for combined $^{1}H/^{19}F$ magnetic resonance (MR) of the human knee at 7.0 Tesla following application of ^{19}F-containing drugs. The benefits of such improvements are in positive alignment with the needs of explorations that are designed to examine the potential of ^{19}F MR to trace and quantify ^{19}F-containing drugs.

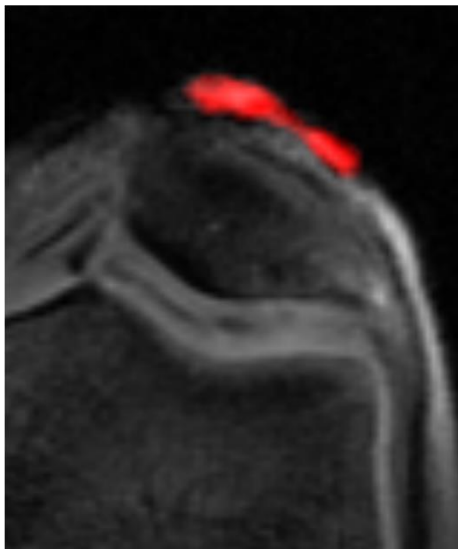

Abstract

Purpose:

To evaluate the feasibility of an eight-channel dual-tuned transceiver surface radiofrequency (RF) coil array for combined $^{1}H/^{19}F$ magnetic resonance (MR) of the human knee at 7.0 Tesla following application of ^{19}F-containing drugs.

Materials and Methods:

The $^{1}H/^{19}F$ RF coil array includes a posterior module with two ^{1}H loop elements and two anterior modules, each consisting of two ^{19}F and one ^{1}H element. The decoupling of neighbor elements is achieved by a shared capacitor. Electromagnetic field simulations were performed to afford uniform transmission fields and to be in accordance with RF safety guidelines. Localized ^{19}F MRS was conducted with 47 and 101 mmol/L of flufenamic acid (FA) – a ^{19}F-containing non-steroidal anti-inflammatory drug (NSAID) – to determine T_1 and T_2 and to study the ^{19}F signal-to-dose relationship. The suitability of the proposed approach for $^{1}H/^{19}F$ MR was examined in healthy subjects.

Results:

Reflection coefficients of each channel were <-17 dB and coupling between channels was <-11 dB. The Q_L/Q_U was <0.5 for all elements. MRS results demonstrated signal stability with 1% of variation. T_1 and T_2 relaxation times changed with concentration of FA: T_1/T_2 = 673/31 ms at 101 mmol/L and T_1/T_2 = 616/26 ms at 47 mmol/L. A uniform signal and contrast across the patella could be observed in proton imaging. The sensitivity of the RF coil enabled localization of FA ointment administrated to the knee with an in-plane spatial resolution of (1.5 × 1.5) mm^2 achieved in a total

scan time of approximately three minutes, which is well suited for translational human studies.

Conclusion:

This study shows the feasibility of combined $^{1}H/^{19}F$ MRI of the knee at 7.0 T and proposes T_1 and T_2 mapping methods for quantifying fluorinated drugs *in vivo*. Further technological developments are necessary to promote real-time bioavailability studies and quantification of ^{19}F-containing medicinal compounds *in vivo*.

Introduction

Fluorine magnetic resonance (^{19}F MR) is a valuable tool for *in vivo* tracking and quantification of fluorine-containing exogenous agents, such as emulsified perfluorcarbon tracer or ^{19}F labeled cells (1-6). The biological abundance of fluorine is negligible. It is mainly present in inorganic form exhibiting very short T_2 relaxation time and therefore low MR detection by MR systems. This virtual absence of fluorine in body tissue yields background free images with complete signal selectivity and specificity. One favorable characteristic of ^{19}F is the relative large chemical shift for organic fluorine compounds spanning a range larger than 250 ppm (7-10), such that resonances of multiple ^{19}F nuclei can be easily separated (11). ^{19}F MR has become increasingly important for small animal imaging in multiple fields of pre-clinical research. Pioneering applications include non-invasive imaging of transplanted neural stem cells (12), early detection of acute allograft rejection (13,14), observation of intracellular oximetry (15), monitoring of cancer therapy (16,17), and assessment of cardiovascular, neurovascular and bowel diseases (5,18-22). Due to the MR characteristics, ^{19}F MR approaches would be potentially valuable for studying the pharmacokinetics of ^{19}F-containing drugs and other compounds (23).

The sensitivity limit for ^{19}F detection constitutes an impediment for translational research and clinical applications (7). The limited number of reports referring to ^{19}F MR in humans is an inherent testament to the practical obstacles of *in vivo* ^{19}F MR (24-28). This state-of-affairs suggests that *in vivo* assessment of ^{19}F content at magnetic field strengths of $B_0 \leq 3.0$ T is challenging, if not elusive, due to signal-to-noise, sensitivity and reproducibility constraints. Realizing these limitations and the intrinsic sensitivity

gain at higher magnetic field strengths (29-40) it is conceptually appealing to pursue *in vivo* ^{19}F MR at ultrahigh field (UHF) strengths ($B_0 \geq 7.0$ T) with dedicated hardware.

Dual-tuned radiofrequency (RF) coils have facilitated ^{19}F MR experiments by enabling co-registration of ^{1}H anatomical images and ^{19}F informational images/spectra without replacing single tuned RF coils or RF coil retuning when switching imaging nucleus, avoiding sample displacement or RF coil sensitivity change. Several approaches can be found in literature that details improvement of this technology for ^{19}F application (20,41-43). In this work we propose a modular dual-tuned ^{1}H/^{19}F eight channel (four proton channels and four fluorine channels) transceiver RF coil array tailored for knee imaging to examine the feasibility of human ^{1}H/^{19}F MR at 7.0 T. Array assembly provides high sensitivity, as it is placed close to the patient, and allows transmit field (B_1^+) shaping by adjusting magnitude and phase of different channels to avoid B_1^+ inhomogeneities at UHF.

Electromagnetic field simulations (EMF) are conducted to carefully assess the performance of the proposed transceiver RF coil array. ^{19}F MR signal-to-dose quantification is performed in phantoms using an ointment containing flufenamic acid (FA) – a ^{19}F-containing non-steroidal anti-inflammatory drug (NSAID). The suitability of the proposed approach for ^{19}F MR following topical application of a flufenamic acid ointment is demonstrated in a pilot volunteer study, as a precursor to broader clinical studies. The merits and limitations of the proposed approach are considered and their implications for *in vivo* drug bioavailability studies at 7.0 T are discussed.

Experimental

RF coil design

An eight-channel transceiver RF coil array tailored for combined ^{19}F and ^{1}H MR of the human knee at 7.0 T was built upon a modular design (44). The RF coil comprises three modules (**Figure 1a**): a posterior module with a curvature radius of 11.5 cm to conform to an average size of the knee's popliteal fossa, and two curved anterior modules (curvature radius = 10 cm) to cover the anterior knee anatomy. The posterior module consists of two rectangular loop elements tuned to ^{1}H (f = 297.0 MHz) (**Figure 1b**). Each posterior element constitutes a loop size of (18 × 9.5) cm^2 to support coverage of the posterior part of the knee. Each anterior module accommodates three square loop elements (**Figure 1c**) arranged into a triangular design to facilitate decoupling of neighboring elements. The two elements located above the knee were tuned to ^{19}F (f = 279.5 MHz). The lateral element was tuned to 297.0 MHz to support coverage and signal homogeneity of anatomic ^{1}H MR. The loop size of each anterior element was set to (5 × 5) cm^2. The modules were assembled to geometrically fit with each other and to accommodate an average geometry of the knee.

The structures shown in **Figure 1** were milled onto printed circuit boards (PCB) using a computer numerical control (CNC) machine Promat S100 (LpKF, Garbsen, Germany). Decoupling between adjacent elements was achieved by a common conductor with a sharing decoupling capacitor (**Figure 1b-c**). The conductor width was set to 10 mm to minimize ohmic losses, and capacitive shortening was used for segmentation of the conductor (**Figure 1b-c**). Non-magnetic and PTFE-free trim

capacitors (Temex-Ceramics, Pessac, France) and ceramic capacitors (American Technical Ceramics Inc., Huntington Station, NY, USA) were used for tuning, matching and subdividing the loops in short sections, less than λ/10. The locations of the capacitors were given by the principal decoupling scheme or were placed to maintain symmetry over all elements. Chip capacitors with a capacitance of 22 pF were used on anterior modules, and chip capacitors with 2.2 and 2.7 pF were used on posterior module. Variable capacitors were used for all shared capacitors and tune/match capacitors.

A cable trap was placed in the feeding cable of each loop element (**Figure 1a**) to suppress unbalanced currents on the coax cables. The cable traps were incorporated into the RF coil casing. The parallel resonant trap circuit is formed by a capacitor and a two-turn solenoid inductor of the feeding coaxial cable itself (45). The capacitor was soldered to the outer conductor of the cable to tune the cable trap to ^{19}F or ^{1}H frequency.

A solid casing was designed for all three modules (**Figure 2a**). The RF coil casing was made from acrylonitrile butadiene styrene (ABS) using a 3D prototyping system (BST 1200es, Dimension Inc., Eden Prairie, MN, USA). The RF coil casing was designed to accommodate and secure all components of the modules including the curvatures of the posterior or anterior RF coil elements. The design was developed with the CAD software Autodesk Inventor 2010 (Autodesk Inc., San Rafael, CA, USA). The casing yields a distance of 10 mm between tissue and the RF coil, avoiding tissue heating caused by high electric fields in the vicinity of conductors and capacitors.

Hardware

The RF characteristics of the RF coil were examined using an 8-channel vector network analyzer (ZVT 8, Rohde & Schwarz, Memmingen, Germany). Measurements of the full set of scattering parameters (S-parameters), which determine the reflection as well as coupling between the loop elements were conducted.

MR experiments were conducted using a 7.0 T whole body MR scanner (Magnetom, Siemens Healthcare, Erlangen, Germany), equipped with (i) a gradient system that offers a maximum slew rate of 200 mT/m/ms and a maximum gradient strength of 40 mT/m (Avanto, Siemens Medical Solutions, Erlangen, Germany) and (ii) an 8 kW single channel RF amplifier (Stolberg HF-Technik AG, Stolberg-Vicht, Germany).

The amplifier output was split into 8 equal-amplitude signals by means of home-built power splitters compiled to a splitting cascade from 1:2, 2:8. For this purpose, Wilkinson power splitters 1:2 and and two 1:4 were used in lumped element design that feature equal intensity and phase differences less than 5° at the outputs. Phase adjustments of each channel were implemented by phase-shifting coaxial cables incorporated in the appropriate position in the power splitting network. All 8 elements were connected to the RF system using multipurpose interface box with transmit/receive switches and integrated low-noise preamplifiers (Stark Contrast, Erlangen, Germany). Compatibility of the proposed RF coil array with a single feeding radiofrequency power amplifier (RFPA) or with an eight channel parallel transmission system is enabled by feeding RF signals into the corresponding stage of the splitting network.

Electromagnetic field simulations

Electromagnetic field simulations including specific absorption rate (SAR) calculations were performed using the FDTD technique of SEMCAD X (Schmid & Partner Engineering AG, Zurich, Switzerland). For this purpose, a virtual model of the experimental version of the RF coil and its casing were placed around the knee of the human voxel model Duke (BMI: 23.1) from the Virtual Family (46). The anatomic position of the voxel model's knee was adapted to ensure a correct distance between the RF coil array and the voxel model. The voxel model was truncated in regions with a negligible influence on the RF fields allowing for a high resolution mesh in the target region (**Figure 2b**). The basic mesh resolution of (3 × 3 × 3) mm^3 was locally refined to (0.3 × 0.4 × 0.7) mm^3 to secure all electrical connections in the RF coil, resulting in a total mesh of 10.3 million cells. The feeding points of the elements were modeled as 50 Ω ports. The resulting S-parameters were exported into Advanced Design System (Agilent Technologies, Santa Clara, CA, USA) where an S-parameter simulation was performed to find the optimal values for all capacitor used for conductor segmentation, tuning, matching and decoupling. The capacitor values were optimized with respect to the S-parameter simulation and were used as a starting point for the practical realization. SAR simulation was performed for the final configuration and phase settings used in *in vivo* measurements. For this, we chose as a total input power of 1 W as reference. Based on the obtained SAR values, the input power used during *in* vivo measurements was adjusted in accordance to IEC 60601-2-33 Ed.3 regulations (47).

Phantom experiments for validation of EMF simulations

A phantom setup consisting of the three modules placed around a cylindrical phantom was used to validate the RF coil model of the EMF simulations. For this purpose, the cylindrical phantom (radius = 90 mm, length = 250 mm) was filled with agarose gel (20 g/L) doped with NaCl (3.33 g/L) and $CuSO_4$ (0.74 g/L), mimicking the tissue dielectric properties of normal healthy knee (ϵ_r = 65, σ = 0.72 S/m). Absolute transmission field (B_1^+) distributions of the individual RF coil elements derived from the EMF simulations were compared to maps of absolute B_1^+ derived from measurements. RF transmission field mapping was conducted for a transversal slice placed through the center of the phantom using a Bloch-Siegert implementation (48) with TR = 100 ms, Fermi pulse, off-center frequency = 4 kHz, scan time = 13 s. The sequence employed double gradient echo acquisitions with echo times TE_1 = 8 ms and TE_2 = 11 ms to enable static magnetic field (B_0) mapping (49). First- and second-order shims were adjusted using volume selective B_0 shimming. B_1^+ mapping was done offline using Bloch simulations in Matlab (MathWorks, Natick, MA, USA), considering B_0 non-uniformities. Due to the proximity of Larmor frequencies of ^1H and ^{19}F, the B_1^+ maps of the ^{19}F elements were acquired at the ^1H frequency and corrected offline by means of the S-parameter values. All absolute B_1^+ values were normalized to the root mean square value of the input power at the feeding point of the loop structure. The resolution of the simulated maps was adapted by interpolation to match the resolution of the measured B_1^+ maps. B_1^+ difference maps were computed pixel-by-pixel by calculating the difference between simulated and measured B_1^+ values as a percentage of the simulated B_1^+ value for each element. For the difference maps, regions with measured values of less than 5 µT/sqrt(kW) were omitted.

Transmission (B_1^+) field shaping

The B_1^+ fields of proton elements 1-4 were extracted at 297.0 MHz from EMF simulations performed on the voxel model's legs, and the fields of fluorine elements 5-8 were extracted at 279.5 MHz. The two sets were post processed with MATLAB using the superposition principle to optimize the homogeneity of the overall proton and fluorine B_1^+ fields of the RF coil. For this purpose, two regions in the center of the patella with a size of (i) (24 × 3 × 3) mm^3 and (ii) (3 × 3 × 3) mm^3 were selected as regions of interest (ROI) for proton and fluorine channels, respectively. The mean phase within the ROI of each channel was compensated so that all the channels were in phase, allowing a constructive interference that yields a more uniform B_1^+ field in the target region. The resulting phase setting was used for all *in vivo* MR studies and for SAR assessment.

^{19}F MR spectroscopy

For ^{19}F MR single voxel spectroscopy (SVS), a SPECIAL (SPin ECho full Intensity Acquired Localized) implementation (50) was employed to detail (i) the transmitter voltage needed to obtain maximum signal for SPECIAL, (ii) reproducibility of ^{19}F signals, (iii) T_1 relaxation, (iv) T_2 relaxation, and (v) the ^{19}F signal-to-dose relationship for a ^{19}F-containing NSAID ointment (flufenamic acid (2-([3-(Trifluoromethyl) phenyl]amino)benzoic acid), STADA Arzneimittel AG, Bad Vilbel, Germany) at 7.0 T.

To determine the correct transmitter voltage needed to achieve the maximum signal for the SPECIAL sequence, a calibration curve was acquired with this sequence varying the reference transmitter voltage, with which the transmitter voltages of all RF pulses are scaled, from 38 V to 56 V on 76 µmol of flufenamic acid contained in an NMR tube (VMR International, Radnor, Pennsylvania, USA, outer diameter = 5 mm, wall thickness = 0.43 mm, height = 50 mm). From the acquired data, the transmitter voltage that provides maximum signal intensity was extrapolated. To examine the signal stability obtained with SVS using SPECIAL, ten independent consecutive measurements were performed with the optimal voltage derived from the calibration curve.

T_1 and T_2 relaxation times were determined for two concentrations of the flufenamic acid (FA) ointment: a) 101 mmol/L FA and b) 47 mmol/L FA. Both samples were contained in NMR tubes (outer diameter = 5 mm, wall thickness = 0.43 mm, height = 50 mm). T_1 and T_2 relaxation times were obtained for a voxel covering the sample using a voxel of size of (7 × 7 × 40) mm^3. For T_1 relaxation time measurements, TR was set to 260, 500, 750, 1000, 1250, 1500, 1750, 2000, 3000, 4000 and 5000 ms with TE = 5.5 ms, total scan time = (33-640) s, number of averages = 128. For T_2 relaxation time measurements, TE was set to = 5.5, 8, 10, 12, 15, 30, 40, 60, 80, 100 and 120 ms for the 101 mmol/L FA sample. For the 47 mmol/L FA sample, TEs of 5.5, 9, 15, 20, 30, 40, 50 and 60 ms were employed. For both FA concentrations, TR was set to 4000 ms with number of averages = 128 and total scan time = 512 s. To calculate the T_1 and T_2 relaxation times for each sample, data were fitted to T_1 and T_2 relaxation equations using MATLAB.

For quantification of the signal-to-dose relationship, a flufenamic acid ointment with a concentration of 101 mmol/L was used. Increasing amounts of FA ranging from 15.3 µmol to 76.5 µmol were achieved by increasing the voxel size of SPECIAL from (7 × 7 × 9) mm^3 to (7 × 7 × 45) mm^3 using increments of 3 mm that correspond to 5 µmol. Measuring parameters were: TR = 2000 ms, TE = 5.5 ms. The number of averages was changed between 1032 and 40, according to the voxel size to assure similar signal-to-noise ratio (SNR) for each measurement resulting in a total scan time ranging in between 512 s and 22 s. The acquired signal intensities were processed and fitted to a linear equation using MATLAB.

Ethics statement

All volunteer studies were performed after due approval by the local ethical committee (registration number DE/CA73/5550/09, Landesamt für Arbeitsschutz, Gesundheitsschutz und technische Sicherheit, Berlin, Germany). Informed written consent was obtained from each volunteer prior to the study.

Pilot study in heathy volunteers

In vivo knee imaging was performed in four healthy subjects (two male, two female, age = 24-31 years, BMI = 23 ± 1 kg/m^2). A small amount of flufenamic acid containing ointment (equivalent to 245 µmol of flufenamic acid) was applied epicutaneously on the region of the patella. High spatial resolution ^1H images of the

knee were acquired using a 2D gradient echo (GRE) technique with reference transmitter voltage = 100 V (corresponding to peak power of 200 W), nominal flip angle = 30°, TR = 10 ms, TE = 2.7 ms, in plane resolution = (0.8 × 0.8) mm^2, slice thickness = 5 mm, number of slices = 5, matrix size = 256 × 256, number of averages = 1 and total scan time = 10.8 s. ^{19}F images of the flufenamic acid ointment were acquired using a 2D GRE sequence and reference transmitter voltage = 65 V (corresponding to peak power of 84.5 W), nominal flip angle = 27°, TR = 90 ms, TE = 1.3 ms, in plane spatial resolution = (1.5 × 1.5) mm^2, slice thickness = 5 mm, number of slices = 5, matrix = 128 × 128, averages = 16, total scan time = 3.06 min. ^{19}F images were threshold-filtered and superimposed to ^{1}H images using ImageJ (NIH, Bethesda, MD, USA).

Results

Hardware and RF characteristics

The modules of the proposed RF coil are lightweight and conform to a broad range of knee geometries. Localized mechanical pressure is averted due to flexible arrangement of the modules. This leads to well perceived patient comfort and easy handling of the three modules. With a height of 31 mm, the modules consume minor space in the effective magnet bore.

The RF coil could be conveniently adapted to various loading conditions governed by the phantom and the healthy subjects by changing the capacitance of the tuning, matching and decoupling of the trim capacitors. Changing the capacitance of the partition capacitors was not required. The S-parameter matrices for both ^{1}H (**Figure 3a**) and ^{19}F (**Figure 3b**) frequencies showed reflection coefficients (S_{ii}) below -17 dB and transmission coefficients (S_{ij}) lower than -11 dB. These values were obtained by averaging over five subjects (2 males, 3 females, age = 24-31, BMI = 21-30 kg/m^2), after tuning and matching the RF coil to one individual subject. It demonstrated that the RF coil is not sensitive to various loads.

The loaded (Q_L) and unloaded quality factor (Q_U) were obtained by loading and unloading the RF coil on a subject. The ratio between these values (Q_L/Q_U) was below 0.5 for all RF coil elements, indicating the dominance of sample noise (**Table 1**). The load power absorption (1- Q_L/Q_U) was found to be 0.52-0.89 (**Table 1**), indicating that most of the RF energy generated by the RF coil is absorbed by the load.

Overall losses from the system RF output to the individual RF coil connectors were determined to be -3.05 dB; the feeding cable from MR system interface to the

Wilkinson power splitters introduced -1.0 dB of loss, the Wilkinson power splitters 1:2 and 1:4 -0.5 dB, the transmit/receive switches -1.5 dB, and coaxial cables -0.05 dB. These losses were found to be in accordance to another RF coil development study at 7.0 T (44) and were considered for the input power calculation. Losses originating from the RF amplifier are calibrated automatically by the MR system, thus they are not considered. Phase cables were manufactured with less than ± 2° phase deviation. The overall variance for the phase adjustment was found to be less than ± 6°.

Validation of EMF simulations in phantoms and B_1^+ *mapping*

The transmission fields obtained from EM simulations of individual RF coil elements placed on the virtual cylindrical phantom were found to be in good quantitative and qualitative agreement with the B_1^+ fields derived from B_1^+ mapping in phantom experiments as illustrated in **Figure 4** for ^{1}H elements 1-4 and ^{19}F elements 5-8. Some artifacts can be detected in the measured B_1^+ maps for elements 1 and 2, due to singularities in the Bloch algorithm when unwrapping phase caused by irregularities within the phantom. The difference map between simulated and measured B_1^+ fields of individual elements is shown as relative difference in percent (**Figure 4**). For the transversal slice of the phantom, the overall mean difference between the mean B_1^+ values obtained for simulations and measurements was found to be between -8.28% and +1.15% for the eight channels. The percentile difference maps demonstrate the validity of the RF coil model and support the credibility of the SAR simulations.

B_1^+ distribution after phase optimization

The phase setting for each individual loop element was determined by transmission field shaping for a ROI placed in the patella. The derived phases (**Table 2**) were implemented in the human voxel model simulations to give rise to a uniform B_1^+ distribution for ^1H and ^{19}F across the region of the patella as outlined in **Figure 5**.

SAR simulations after phase optimization

The 10 g averaged local SAR distribution was determined for all ^1H and ^{19}F elements using the phases derived from transmission field shaping (**Figure 6**). The maximum 10 g averaged local SAR for the four proton loop elements at ^1H frequency was found to be 0.65 W/kg for 1 W of input power. Using the same power settings, the maximum 10 g averaged SAR for the four fluorine elements at ^{19}F frequency was 1.76 W/kg. Considering -3.05 dB of hardware losses, these findings were used to limit the maximum input power used in *in vivo* experiments to 22 W, to stay within the 20 W/kg SAR limit specified by the IEC guidelines for body extremities at normal operating mode (47). The first and second level controlled mode given by the IEC guidelines (47) were not used in the *in vivo* applications which limits the maximum local 10 g SAR to 40 W/kg and thus preserves a safety margin of factor 2.

^{19}F MR spectroscopy

To determine the correct transmitter voltage, a calibration curve was acquired using reference transmitter voltages ranging from 38 V to 56 V (corresponds to peak power of 28.9 to 62.7 W). For this purpose, SVS using the fluorine loop elements (5-8)

together with an NMR tube containing 76 µmol FA was performed. The reference transmitter voltage for obtaining maximum ^{19}F signal using SPECIAL sequence was found to be 44 V (corresponding to 38.8 W peak power) (**Figure 7a**).

To determine the reproducibility of the ^{19}F signal, ten acquisitions were then performed using the transmitter voltage of 44 V. For this reference transmitter voltage, a mean signal intensity of 3.94 ± 0.04 (a. u.) was observed for the ^{19}F signal. This translates into a signal variation of 1% (**Figure 7b**)**.**

To scrutinize the ^{19}F signal-to-dose relationship for flufenamic acid, SVS was performed. For this purpose, increasing amounts of FA ranging from 15.3 µmol to 76.5 µmol were used. The signal-to-dose quantification curve is shown in **Figure 7c**. The slope of the curve yielded a signal-to-dose relationship of 0.05 arbitrary signal per µmol FA with a linear regression coefficient of 0.99.

T_1 and T_2 relaxation times were examined for FA concentrations of 101 mmol/L and 47 mmol/L. A longitudinal relaxation time of T_1 = 616 ms was observed for a concentration of 47 mmol/L FA (**Figure 8a**). A concentration of 101 mmol/L FA yielded T_1 = 673 ms (**Figure 8a**). A transversal relaxation time of T_2 = 31 ms was deduced for a concentration of 101 mmol/L FA. A concentration of 47 mmol/L FA revealed a T_2 relaxation time of 26 ms (**Figure 8b**).

Pilot study in healthy volunteers

For the pilot study in healthy volunteers, all eight elements of the proposed modular $^{1}H/^{19}F$ transceiver array were exploited. **Figure 9** surveys transversal ^{1}H and ^{19}F views of the knee for all subjects. The RF coil design supported anatomic ^{1}H 2D GRE imaging which provided uniform signal and contrast across the patella by applying the phase settings derived from the transmission field shaping procedure. A spatial resolution of (0.8 × 0.8 x 5.0) mm^3 was achieved in a scan time of 11 s (**Figure 9,** left column). The proposed transceiver array facilitated ^{19}F 2D GRE imaging of the FA ointment using a spatial resolution as high as (1.5 × 1.5 x 5.0) mm^3, which was accomplished in a total scan time of approximately three minutes (**Figure 9**, middle column). The overlay of ^{19}F images in red and ^{1}H anatomical images in gray scale provides visualization of the FA ointment at the area of topical application (**Figure 9,** right column).

Discussion

This study adds to the literature by demonstrating that the proposed modular eight channel $^{1}H/^{19}F$ transceiver RF coil array supports proton and fluorine MR of the human knee and fluorinated drugs at 7.0 Tesla. The sensitivity of the proposed RF coil array enabled ^{19}F localization following epicutaneous administration of a ^{19}F-containing NSAID ointment to the human knee. The in-plane spatial resolution was as high as (1.5 × 1.5) mm^2. This spatial fidelity was accomplished in a total scan time of approximately three minutes, which is very well suited for translational human studies and for clinical applications. These findings indicate that ^{19}F MR may represent a potentially useful resource for studying the distribution and bioavailability of ^{19}F-containing drugs in clinical trials.

Beside patient comfort and flexibility to accommodate a broad range of knee sizes, the RF characteristics of the proposed RF coil are encouraging and suggest that subject-specific tuning and matching may not be necessary when used in a clinical setting. However, as every sensitivity gain is crucial for ^{19}F MR, the RF coil should be properly tuned and matched for each loading condition. This could be conveniently done on the phantom and different subjects studied here by changing the capacitance of the tuning, matching and decoupling of the trim capacitors. The Q-factor ratio of all elements was below 0.5, indicating a sample noise dominance, which is desirable for achieving higher SNR.

The proposed transceiver array encourages further explorations into densely packed multi-channel transceiver RF coil arrays tailored for ^{19}F MR. With appropriate single or multi transmit systems, one might envisage the implementation of ^{19}F RF coil

arrays tailored for knee MRI with even more than eight transmit/receive elements. This vision continues to motivate new research on integrated multi-channel systems (51) and on RF coil design together with explorations into ideal current patterns (52) in order to yield the best possible SNR for UHF-MR. The field is in a state of creative flux and future solutions will involve designs that use different building blocks for signal transmission and reception in order to balance the constraints dictated by sensitivity, depth penetration, transmission field uniformity and SNR (53). In this context, a recent report suggested the combination of dipole antenna for excitation and loop elements for reception (53). In addition, recent considerations outlined that loop and dipole current patterns contribute equally to ultimate intrinsic SNR at 7.0 T (52,54). For field strengths of $B_0 \geq 9.4$ T, current patterns are dominated by linear (dipole type) current patterns (52,54), which provides motivation for shifting the weight to dipoles versus loop elements. With this in mind, moving toward magnetic field strengths of $B_0 = 9.4$ T and higher holds the promise for improved spatial resolution and sensitivity during quantitative ^{19}F MR studies.

Our ^{19}F SVS phantom studies with flufenamic acid showed a steady ^{19}F signal over a series of independent measurements with a signal variability of 1%. A closer examination revealed a detection limit of 15.3 µmol corresponding to ~9.2×10^{18} ^{19}F spins for the proposed setup. Notwithstanding this success, SVS at 7.0 T remains challenging since it is prone to B_0 inhomogeneities, requires extra shimming adjustments and builds upon sophisticated offline post-processing. B_0 inhomogeneities at 7.0 T also make SVS vulnerable to partial volume effects. One option to overcome this shortcoming could be the use of multi-voxel spectroscopy (or chemical shift

imaging) that provides spatially resolved results (55) though at the expense of lower SNR (56). For more complex ^{19}F molecular structures, optimized sequences that minimize J coupling effects and provide large RF bandwidths to reduce chemical shift artifacts will be required. One possible approach could be to perform sine-bell acquisition-weighted chemical shift imaging with selective refocusing pulses (5).

Our phantom studies showed changes in T_1 and T_2 relaxation times with increasing concentrations of flufenamic acid. An increase in FA concentration of more than 200% resulted in an increase in T_1 (109%) and T_2 (120%) relaxation times. Other than changes in ^{19}F concentration, spin-lattice relaxation rates (R_1) of fluorinated compounds were also shown to be dependent on temperature and magnetic field strength (57). In biological tissue, T_2 relaxation times of fluorinated anesthetic were reported to correlate with temperature and anesthetic potency (58). The binding capacity of drug to macromolecular sites also influences changes in T_1 values; competitive binding for common binding sites strongly reduces the T_1 relaxation for ^{19}F drugs (59). Therefore T_1 and T_2 mapping techniques can also be considered as important tools for detailing the profile of ^{19}F-containing compounds.

NSAIDs have been shown to have anti-inflammatory, analgesic, and antipyretic effects and when applied topically they are believed to reduce inflammation in muskuloskeletal disorders. These compounds have been shown to penetrate the human skin but no human *in vivo* studies have been carried out so far to study the distribution, let alone quantification, of active compound at the site of injury where the compound is acting. In this study we demonstrated the feasibility of tracking ^{19}F-containing NSAID *in vivo* at 7.0 T, which encourages further studies in patients suffering

from inflammatory conditions. It is conceivable, that the concentration of drug ultimately penetrating the skin to reach its site of action (in the case of NSAIDs, areas of inflammation) might be close to or even lower than the detection limit. In biological tissue, the NMR properties of ^{19}F-containing drugs are also expected to change as has been previously reported for T_1 (59) and T_2 (58) relaxation times. This is due to several factors such as changes in the environment but also pharmacokinetic (e.g. degradation of parent compound) as well as pharmacodynamic processes (e.g. protein binding). In contrast to the present volunteer study, the ^{19}F-containing topical NSAID is commonly applied up to three times daily in patients and over longer periods of time; an accumulation of active compound at its site of action is to be expected. This potentially increases the locally available quantities of drugs *in vivo*. However, it is still likely that the concentration of drug at the site of action to be too low for detection. The low availability of drug and low ^{19}F signal sensitivity are indeed main limitations for drug targeting studies at the moment. In our healthy volunteer studies ^{19}F 2D GRE imaging of substantial quantities of ^{19}F-containing drug was achieved in a total scan time of approximately three minutes, which is well suited for translational human studies. Although the scan time could be moderately increased to accommodate for averaging in order to increase ^{19}F signal, increasing the total scan time is generally undesirable. Apart from issues concerning patient comfort, longer scan sessions are also prone to motion artifacts. Especially for high spatially-resolved SVS quantification inaccuracies might also arise. Evolving MR measuring techniques such as compressed sensing might be valuable in the future to offset speed constraints for *in vivo* ^{19}F MRI (60). Improved ^{19}F spectroscopic techniques, perhaps less prone to B_0 inhomogeneities and

chemical shift artifacts, will be a further challenge to overcome in order to quantify ^{19}F drug *in vivo*. B_1^+ field compensation techniques will be necessary to avoid possible incorrect ^{19}F MR drug quantification as a result of B_1^+ inhomogeneities when comparing drug spectra at the site of interest with standard drug reference spectra (61,62).

Although, accessing *in vivo* distribution and quantification of ^{19}F-contained drugs presents several challenges, the preliminary findings of this ^{19}F MR study at 7.0 T are encouraging and point towards the prospect of applying ^{19}F MR and NSAID therapy to the field of theranostics with the ultimate goal to visualize and measure the concentration along with providing dosage guiding of a therapeutically-active compound reaching the inflammatory site in rheumatoid arthritis patients. While this is, for the moment, merely a *gedankenexperiment*, it continues to motivate new research and encourages further studies with patients suffering from inflammatory conditions. These pioneering efforts include ^{19}F MR visualization (i) of collagen induced arthritic inflammation in small rodents upon invasive administration of a perfluorcarbon contrast agent as a means of studying therapeutic response (63) and (ii) of arthritic rabbit knees following intra-articular injection of a perfluoro-15-crown-5-ether emulsion (41). In light of a pioneering report on labeling dendritic cells (DCs) with a clinical-grade ^{19}F label (perfluoro dialkyl ether, CS-1000, Celsense) and reintroduction in cancer patients (26), the modular design of our RF coil technology could be adapted for DC imaging with higher sensitivity at 7.0 T. In the recent proof-of-concept study, DCs were visualized at their site of application using combined ^{19}F and ^{1}H MR imaging at 3.0 T (26). Although DCs could be clearly visualized at their site of application, there was no MRI evidence of cell accumulation in the draining lymph nodes (26), possibly due to cell densities in

these regions being on the order of, or below, the cell detection limit threshold for the experimental configuration employed (26).

In conclusion, this study showed the feasibility of ^{19}F MRI of the knee after epicutaneous application of a ^{19}F contained NSAID. The proposed modular eight channel ^{1}H/^{19}F transceiver RF coil array contributes to the technological basis for the clinical assessment of biodistribution and bioavailability of ^{19}F-containing drugs. The results underscore the challenges of fluorine MR in humans and demonstrate that these issues can be offset by using tailored RF coil hardware. The benefits of such improvements would be in positive alignment with the needs of explorations that are designed to examine the potential of ^{19}F MR to trace and quantify ^{19}F-containing drugs. As 7.0 T UHF-MR applications become increasingly used for research, they should help to advance the capabilities of *in vivo* ^{19}F MR for the assessment of the metabolic fate of ^{19}F-containing drugs.

Acknowledgments

The authors would like to thank Maria del Mar Miñana and her team from Schmid & Partner Engineering AG (Zurich, Switzerland) for their support on EMF simulations.

References

1. Srinivas M, Heerschap A, Ahrens ET, Figdor CG, de Vries IJ. (19)F MRI for quantitative in vivo cell tracking. Trends in biotechnology 2010;28(7):363-370.
2. Bonetto F, Srinivas M, Heerschap A, Mailliard R, Ahrens ET, Figdor CG, de Vries IJ. A novel (19)F agent for detection and quantification of human dendritic cells using magnetic resonance imaging. International journal of cancer Journal international du cancer 2011;129(2):365-373.
3. Helfer BM, Balducci A, Nelson AD, Janjic JM, Gil RR, Kalinski P, de Vries IJ, Ahrens ET, Mailliard RB. Functional assessment of human dendritic cells labeled for in vivo (19)F magnetic resonance imaging cell tracking. Cytotherapy 2010;12(2):238-250.
4. Waiczies H, Lepore S, Janitzek N, Hagen U, Seifert F, Ittermann B, Purfürst B, Pezzutto A, Paul F, Niendorf T. Perfluorocarbon particle size influences magnetic resonance signal and immunological properties of dendritic cells. PloS one 2011;6(7):e21981.
5. Jacoby C, Temme S, Mayenfels F, Benoit N, Krafft MP, Schubert R, Schrader J, Flogel U. Probing different perfluorocarbons for in vivo inflammation imaging by 19F MRI: image reconstruction, biological half-lives and sensitivity. NMR in biomedicine 2014;27(3):261-271.
6. Ahrens ET, Zhong J. In vivo MRI cell tracking using perfluorocarbon probes and fluorine-19 detection. NMR in biomedicine 2013;26(7):860-871.
7. Chen J, Lanza GM, Wickline SA. Quantitative magnetic resonance fluorine imaging: today and tomorrow. Wiley interdisciplinary reviews Nanomedicine and nanobiotechnology 2010;2(4):431-440.
8. Günther H. NMR spectroscopy: basic principles, concepts and applications in chemistry: John Wiley & Sons; 2013.
9. Ruiz-Cabello J, Barnett BP, Bottomley PA, Bulte JW. Fluorine (19F) MRS and MRI in biomedicine. NMR in biomedicine 2011;24(2):114-129.
10. Wolf W, Presant CA, Waluch V. < sup> 19</sup> F-MRS studies of fluorinated drugs in humans. Advanced drug delivery reviews 2000;41(1):55-74.
11. Dolbier WR. Guide to fluorine NMR for organic chemists: John Wiley & Sons; 2009.
12. Bible E, Dell'Acqua F, Solanky B, Balducci A, Crapo PM, Badylak SF, Ahrens ET, Modo M. Non-invasive imaging of transplanted human neural stem cells and ECM scaffold remodeling in the stroke-damaged rat brain by< sup> 19</sup> F-and diffusion-MRI. Biomaterials 2012;33(10):2858-2871.
13. Hitchens TK, Ye Q, Eytan DF, Janjic JM, Ahrens ET, Ho C. 19F MRI detection of acute allograft rejection with in vivo perfluorocarbon labeling of immune cells. Magnetic Resonance in Medicine 2011;65(4):1144-1153.
14. Flögel U, Su S, Kreideweiss I, Ding Z, Galbarz L, Fu J, Jacoby C, Witzke O, Schrader J. Noninvasive detection of graft rejection by in vivo 19F MRI in the early stage. American Journal of Transplantation 2011;11(2):235-244.
15. Kadayakkara DK, Janjic JM, Pusateri LK, Young WB, Ahrens ET. In vivo observation of intracellular oximetry in perfluorocarbon-labeled glioma cells and

chemotherapeutic response in the CNS using fluorine-19 MRI. Magnetic Resonance in Medicine 2010;64(5):1252-1259.
16. Weibel S, Basse-Luesebrink TC, Hess M, Hofmann E, Seubert C, Langbein-Laugwitz J, Gentschev I, Sturm VJF, Ye Y, Kampf T. Imaging of intratumoral inflammation during oncolytic virotherapy of tumors by 19F-magnetic resonance imaging (MRI). PloS one 2013;8(2):e56317.
17. Bartusik D, Tomanek B. Application of< sup> 19</sup> F magnetic resonance to study the efficacy of fluorine labeled drugs in the three-dimensional cultured breast cancer cells. Archives of biochemistry and biophysics 2010;493(2):234-241.
18. Jacoby C, Borg N, Heusch P, Sauter M, Bönner F, Kandolf R, Klingel K, Schrader J, Flögel U. Visualization of immune cell infiltration in experimental viral myocarditis by 19F MRI in vivo. Magnetic Resonance Materials in Physics, Biology and Medicine 2014;27(1):101-106.
19. Flögel U, Ding Z, Hardung H, Jander S, Reichmann G, Jacoby C, Schubert R, Schrader J. In vivo monitoring of inflammation after cardiac and cerebral ischemia by fluorine magnetic resonance imaging. Circulation 2008;118(2):140-148.
20. Waiczies H, Lepore S, Drechsler S, Qadri F, Purfürst B, Sydow K, Dathe M, Kühne A, Lindel T, Hoffmann W. Visualizing brain inflammation with a shingled-leg radio-frequency head probe for 19F/1H MRI. Scientific reports 2013;3.
21. Kadayakkara DK, Ranganathan S, Young W-B, Ahrens ET. Assaying macrophage activity in a murine model of inflammatory bowel disease using fluorine-19 MRI. Laboratory Investigation 2012;92(4):636-645.
22. Waiczies H, Millward JM, Lepore S, Infante-Duarte C, Pohlmann A, Niendorf T, Waiczies S. Identification of cellular infiltrates during early stages of brain inflammation with magnetic resonance microscopy. PloS one 2012;7(3):e32796.
23. Liu X, Kevin Li S, Jeong E-K. Ocular pharmacokinetic study of a corticosteroid by< sup> 19</sup> F MR. Experimental eye research 2010;91(3):347-352.
24. Bolo NR, Hodé Y, Macher JP. Long-term sequestration of fluorinated compounds in tissues after fluvoxamine or fluoxetine treatment: a fluorine magnetic resonance spectroscopy study in vivo. Magnetic Resonance Materials in Physics, Biology and Medicine 2004;16(6):268-276.
25. Bolo NR, Hode Y, Nedelec J-F, Laine E, Wagner G, Macher J-P. Brain Pharmacokinetics and Tissue Distribution In Vivo of Fluvoxamine and Fluoxetine by Fluorine Magnetic Resonance Spectroscopy. Neuropsychopharmacology 2000;23(4):428-438.
26. Ahrens ET, Helfer BM, O'Hanlon CF, Schirda C. Clinical cell therapy imaging using a perfluorocarbon tracer and fluorine-19 MRI. Magnetic Resonance in Medicine 2014.
27. Bilecen D, Schulte A-C, Kaspar A, Küstermann E, Seelig J, Elverfeldt Dv, Scheffler K. Detection of the non-steroidal anti-inflammatory drug niflumic acid in humans: a combined 19F-MRS in vivo and in vitro study. NMR in biomedicine 2003;16(3):144-151.

28. Klomp DW, van Laarhoven HW, Kentgens AP, Heerschap A. Optimization of localized 19F magnetic resonance spectroscopy for the detection of fluorinated drugs in the human liver. Magnetic Resonance in Medicine 2003;50(2):303-308.
29. Niendorf T, Graessl A, Thalhammer C, Dieringer MA, Kraus O, Santoro D, Fuchs K, Hezel F, Waiczies S, Ittermann B, Winter L. Progress and promises of human cardiac magnetic resonance at ultrahigh fields: a physics perspective. J Magn Reson 2013;229:208-222.
30. Kraff O, Fischer A, Nagel AM, Mönninghoff C, Ladd ME. MRI at 7 tesla and above: Demonstrated and potential capabilities. Journal of Magnetic Resonance Imaging 2014.
31. Duyn JH. The future of ultra-high field MRI and fMRI for study of the human brain. NeuroImage 2012;62(2):1241-1248.
32. Uğurbil K, Adriany G, Andersen P, Chen W, Garwood M, Gruetter R, Henry P-G, Kim S-G, Lieu H, Tkac I. Ultrahigh field magnetic resonance imaging and spectroscopy. Magnetic resonance imaging 2003;21(10):1263-1281.
33. Moser E, Stahlberg F, Ladd ME, Trattnig S. 7-T MR—from research to clinical applications? NMR in biomedicine 2012;25(5):695-716.
34. Regatte RR, Schweitzer ME. Ultra-high-field MRI of the musculoskeletal system at 7.0T. Journal of magnetic resonance imaging : JMRI 2007;25(2):262-269.
35. Ladd ME. High-field-strength magnetic resonance: potential and limits. Topics in Magnetic Resonance Imaging 2007;18(2):139-152.
36. Niendorf T, Sodickson DK, Krombach GA, Schulz-Menger J. Toward cardiovascular MRI at 7 T: clinical needs, technical solutions and research promises. European radiology 2010;20(12):2806-2816.
37. Uğurbil K. The road to functional imaging and ultrahigh fields. NeuroImage 2012;62(2):726-735.
38. Trattnig S, Zbýň Š, Schmitt B, Friedrich K, Juras V, Szomolanyi P, Bogner W. Advanced MR methods at ultra-high field (7 Tesla) for clinical musculoskeletal applications. European radiology 2012;22(11):2338-2346.
39. van der Kolk AG, Hendrikse J, Zwanenburg JJ, Visser F, Luijten PR. Clinical applications of 7T MRI in the brain. European journal of radiology 2013;82(5):708-718.
40. Ugurbil K. Magnetic Resonance Imaging at Ultrahigh Fields. 2014.
41. Hockett FD, Wallace KD, Schmieder AH, Caruthers SD, Pham CT, Wickline SA, Lanza GM. Simultaneous dual frequency and open coil imaging of arthritic rabbit knee at 3T. Medical Imaging, IEEE Transactions on 2011;30(1):22-27.
42. Hu L, Hockett FD, Chen J, Zhang L, Caruthers SD, Lanza GM, Wickline SA. A generalized strategy for designing 19F/1H dual-frequency MRI coil for small animal imaging at 4.7 Tesla. Journal of Magnetic Resonance Imaging 2011;34(1):245-252.
43. Ha S, Hamamura MJ, Nalcioglu O, Muftuler LT. A PIN diode controlled dual-tuned MRI RF coil and phased array for multi nuclear imaging. Physics in medicine and biology 2010;55(9):2589.
44. Graessl A, Renz W, Hezel F, Dieringer MA, Winter L, Oezerdem C, Rieger J, Kellman P, Santoro D, Lindel TD, Frauenrath T, Pfeiffer H, Niendorf T. Modular 32-channel transceiver coil array for cardiac MRI at 7.0T. Magnetic resonance in

medicine : official journal of the Society of Magnetic Resonance in Medicine / Society of Magnetic Resonance in Medicine 2014;72(1):276-290.
45. Thalhammer C, Renz W, Winter L, Hezel F, Rieger J, Pfeiffer H, Graessl A, Seifert F, Hoffmann W, von Knobelsdorff-Brenkenhoff F. Two-Dimensional sixteen channel transmit/receive coil array for cardiac MRI at 7.0 T: Design, evaluation, and application. Journal of Magnetic Resonance Imaging 2012;36(4):847-857.
46. Christ A, Kainz W, Hahn EG, Honegger K, Zefferer M, Neufeld E, Rascher W, Janka R, Bautz W, Chen J. The Virtual Family—development of surface-based anatomical models of two adults and two children for dosimetric simulations. Physics in medicine and biology 2010;55(2):N23.
47. International-Electrotechnical-Commission. Medical electrical equipment.-Part 2-33: particular requirements for the basic safety and essential performance of magnetic resonance equipment for medical diagnosis: IEC; 2010.
48. Sacolick LI, Wiesinger F, Hancu I, Vogel MW. B1 mapping by Bloch-Siegert shift. Magnetic resonance in medicine : official journal of the Society of Magnetic Resonance in Medicine / Society of Magnetic Resonance in Medicine 2010;63(5):1315-1322.
49. Schneider E, Glover G. Rapid in vivo proton shimming. Magnetic Resonance in Medicine 1991;18(2):335-347.
50. Mekle R, Mlynárik V, Gambarota G, Hergt M, Krueger G, Gruetter R. MR spectroscopy of the human brain with enhanced signal intensity at ultrashort echo times on a clinical platform at 3T and 7T. Magnetic Resonance in Medicine 2009;61(6):1279-1285.
51. Poulo L, Alon L, Deniz C, Haefner R, Sodickson D, Stoeckel B, Zhu Y. A 32-Channel Parallel Exciter/Amplifier Transmit System for 7T Imaging. In: ISMRM, editor. Proc Intl Soc Mag Reson Med 19; 2011. p 1867.
52. Lattanzi R, Sodickson DK. Ideal current patterns yielding optimal signal-to-noise ratio and specific absorption rate in magnetic resonance imaging: computational methods and physical insights. Magnetic resonance in medicine : official journal of the Society of Magnetic Resonance in Medicine / Society of Magnetic Resonance in Medicine 2012;68(1):286-304.
53. Wiggins GJ, Zhang B, Lattanzi R, Chen GM, Sodickson DK. The Electric Dipole Array: An Attempt to Match the Ideal Current Pattern for Central SNR at 7 Tesla. 2012. p 541.
54. Graham Charles Wiggins1 BZ, Riccardo Lattanzi1, Gang Chen2, and Daniel Sodickson. The Electric Dipole Array: An Attempt to Match the Ideal Current Pattern for Central SNR at 7 Tesla. Proc Intl Soc Mag Reson Med 20 2012.
55. Alvarez-Linera J. 3 T MRI: Advances in brain imaging. European Journal of Radiology 2008;67(3):415-426.
56. Maudsley AA, Hilal SK, Perman WH, Simon HE. Spatially resolved high resolution spectroscopy by “four-dimensional” NMR. Journal of Magnetic Resonance (1969) 1983;51(1):147-152.
57. Kadayakkara DK, Damodaran K, Hitchens TK, Bulte JW, Ahrens ET. (19)F spin-lattice relaxation of perfluoropolyethers: Dependence on temperature and magnetic field strength (7.0-14.1T). J Magn Reson 2014;242:18-22.

58. Evers AS, Haycock JC, Andre d'Avignon D. The potency of fluorinated ether anesthetics correlates with their 19F spin-spin relaxation times in brain tissue. Biochemical and biophysical research communications 1988;151(3):1039-1045.
59. Dzik-Jurasz A, Leach M, Rowland IJ. Investigation of microenvironmental factors influencing the longitudinal relaxation times of drugs and other compounds. Magnetic resonance imaging 2004;22(7):973-982.
60. Zhong J, Mills PH, Hitchens TK, Ahrens ET. Accelerated fluorine-19 MRI cell tracking using compressed sensing. Magnetic resonance in medicine : official journal of the Society of Magnetic Resonance in Medicine / Society of Magnetic Resonance in Medicine 2013;69(6):1683-1690.
61. Vovk U, Pernus F, Likar B. A review of methods for correction of intensity inhomogeneity in MRI. Medical Imaging, IEEE Transactions on 2007;26(3):405-421.
62. Goette MJ, Lanza GM, Caruthers SD, Wickline SA. Improved quantitative 19F MR molecular imaging with flip angle calibration and B1-mapping compensation. Journal of Magnetic Resonance Imaging 2014.
63. Balducci A, Helfer BM, Ahrens ET, O'Hanlon CF, Wesa AK. Visualizing arthritic inflammation and therapeutic response by fluorine-19 magnetic resonance imaging (19F MRI). J Inflammation (London, UK) 2012;9(1):24-34.

Tables

Table 1. Loaded quality factor (Q_L), unloaded Q factor (Q_U), ratio between Q_L and Q_U (Q_L/Q_U) and load power absorption (1- Q_L/Q_U) for each RF coil element.

Nucleus	Element #	Q loaded (Q_L)	Q unloaded (Q_U)	Q_L/Q_U	1- Q_L/Q_U
^{1}H	1	12.91	59.4	0.22	0.78
	2	17.7	37.1	0.48	0.52
	3	15.4	62.5	0.25	0.75
	4	15.4	99.0	0.16	0.84
^{19}F	5	25.4	93.2	0.27	0.73
	6	29.4	223.6	0.13	0.87
	7	27.3	248.4	0.11	0.89
	8	27.3	124.2	0.22	0.78

Table 2. Phase setting of each RF coil element.

Nucleus	Element #	Phase
^{1}H	1	38°
	2	110°
	3	0°
	4	190°
^{19}F	5	77°
	6	160°
	7	208°
	8	313°

Figures captions

Figure 1

a) Photograph of the proposed modular, eight channel transceiver RF coil array with the top casing being removed. The figure includes element nomenclature (numbers 1-8) and nuclei ($^{1}H/^{19}F$) identification. b) Basic loop structure for the posterior module including capacitor placement and capacitor values. c) Basic loop structure for the anterior module including capacitor placement and capacitor values. C_D – decoupling capacitor, C_M – matching capacitor, C_T – tuning capacitor, trim – trim capacitors (1-13 pF).

Figure 2

a) Photograph of the RF coil array conforming to the knee of a volunteer. b) An accurate model of the RF coil and the lower legs of the voxel model “Duke” used (46) for the electromagnetic field simulations.

Figure 3

Synopsis of the results derived from the assessment of the RF characteristics of the eight channel transceive $^{1}H/^{19}F$ RF coil array including S-parameter matrix averaged over five subjects (a) at ^{1}H frequency (f = 297.0 MHz), and (b) at ^{19}F frequency (f = 279.5 MHz).

Figure 4

Comparison of simulated and measured B_1^+ maps for each element loop of the proposed RF coil array using a cylindrical phantom setup. a) For B_1^+ evaluation, transversal slices of the cylindrical phantom were positioned in alignment with the center of the loop elements. Left column: Simulated and measured B_1^+ maps of the ^1H loop elements. B_1^+ was normalized to maximum B_1^+ of each element. Middle column: Simulated and measured B_1^+ maps of the ^{19}F loop elements. B_1^+ was normalized to maximum B_1^+ of each element. Due to the proximity of Larmor frequencies of ^1H and ^{19}F, the B_1^+ maps of the ^{19}F elements were acquired at the ^1H frequency and corrected offline by means of the S-parameter values. Right column: B_1^+ difference maps of the proton and fluorine elements. The measured maps were subtracted pixel-by-pixel from the simulated maps and normalized to the simulated maps. The results demonstrate the qualitative and quantitative agreement between the numerical simulations and the measurements. b) Positioning of the transversal slices with respect to the coil elements and to the phantom (coronal view). The blue dashed rectangle represents the phantom, the black dotted lines the transversal slice positioning and the numbers refer to element nomenclature.

Figure 5

Axial, sagittal and coronal views of the B_1^+ distribution of the ^1H and ^{19}F elements of the proposed transceiver array for the male human voxel model Duke (46). To guide the eye, the loop elements of the anterior modules are shown in light grey and the loop

elements of the posterior module are marked in light green. The numbers refer to the element nomenclature. Phase setting of the elements was set to: element 1 = 38°, element 2 = 110°, element 3 = 0°, element 4 = 190°, element 5 = 77°, element 6 = 160°, element 7 = 208° and element 8 = 313°. The dotted lines describe the slices from which the B_1^+ distribution views were obtained.

Figure 6

Axial, sagittal and coronal views of the maximum projection plots of the local 10 g averaged SAR distribution for the male human voxel model Duke based on the phase setting: element 1 = 38°, element 2 = 110°, element 3 = 0°, element 4 = 190°, element 5 = 77°, element 6 = 160°, element 7 = 208° and element 8 = 313°. The loop elements of the anterior parts are shown in light grey and the loop elements of the posterior part are marked in in light green. The numbers refer to element nomenclature. The dotted lines describe the slices from which the views are obtained.

Figure 7

Synopsis of the phantom experiments using single voxel spectroscopy with a SPECIAL implementation (50). a) Transmitter voltage calibration curve showing signal intensity versus transmitter voltage and the extrapolated required transmitter voltage that provides maximum signal intensity for the SPECIAL sequence. b) Ten consecutive independent measurements with a transmitter voltage of 44 V. A mean signal intensity

of 3.94 ± 0.04 (a. u.) was observed for the ^{19}F signal. c) Signal-to-dose quantification curve of the ointment containing flufenamic acid (FA).

Figure 8

Synopsis of the relaxation time measurements. T_1 (a) and T_2 (b) relaxation curves of concentrations 101 mmol/L and 47 mmol/L of FA.

Figure 9

Synopsis of the *in vivo* pilot study. Left: ^{1}H axial views derived from gradient echo imaging the knees of four healthy subjects. A spatial resolution of (0.8 × 0.8 × 5.0) mm^3 was achieved. Center: Corresponding axial views of threshold filtered ^{19}F GRE images following topical application of the FA ointment. A spatial resolution of (1.5 × 1.5 × 5.0) mm^3 was accomplished. Right: Overlay of the ^{1}H (grey scale) and ^{19}F images (red).

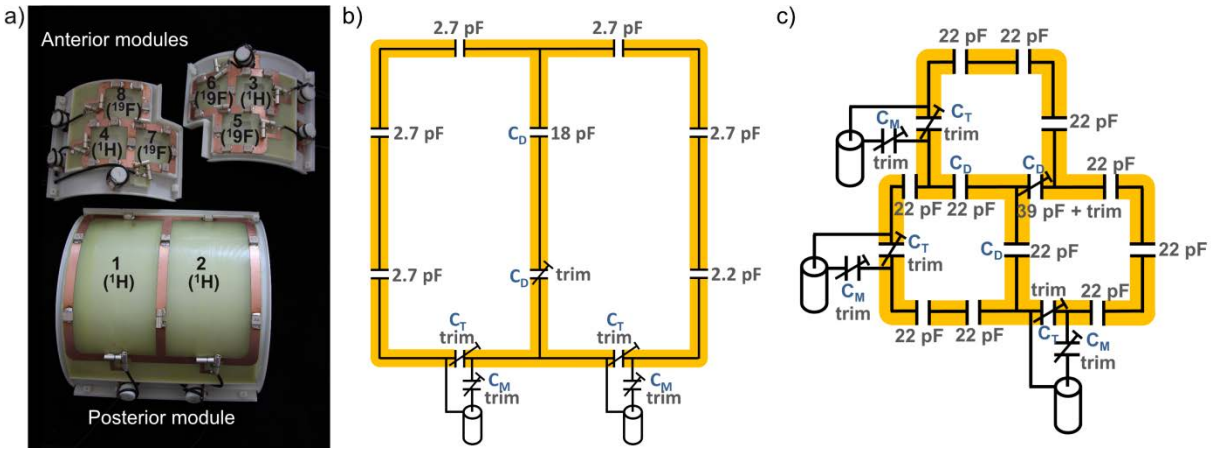

Figure 1

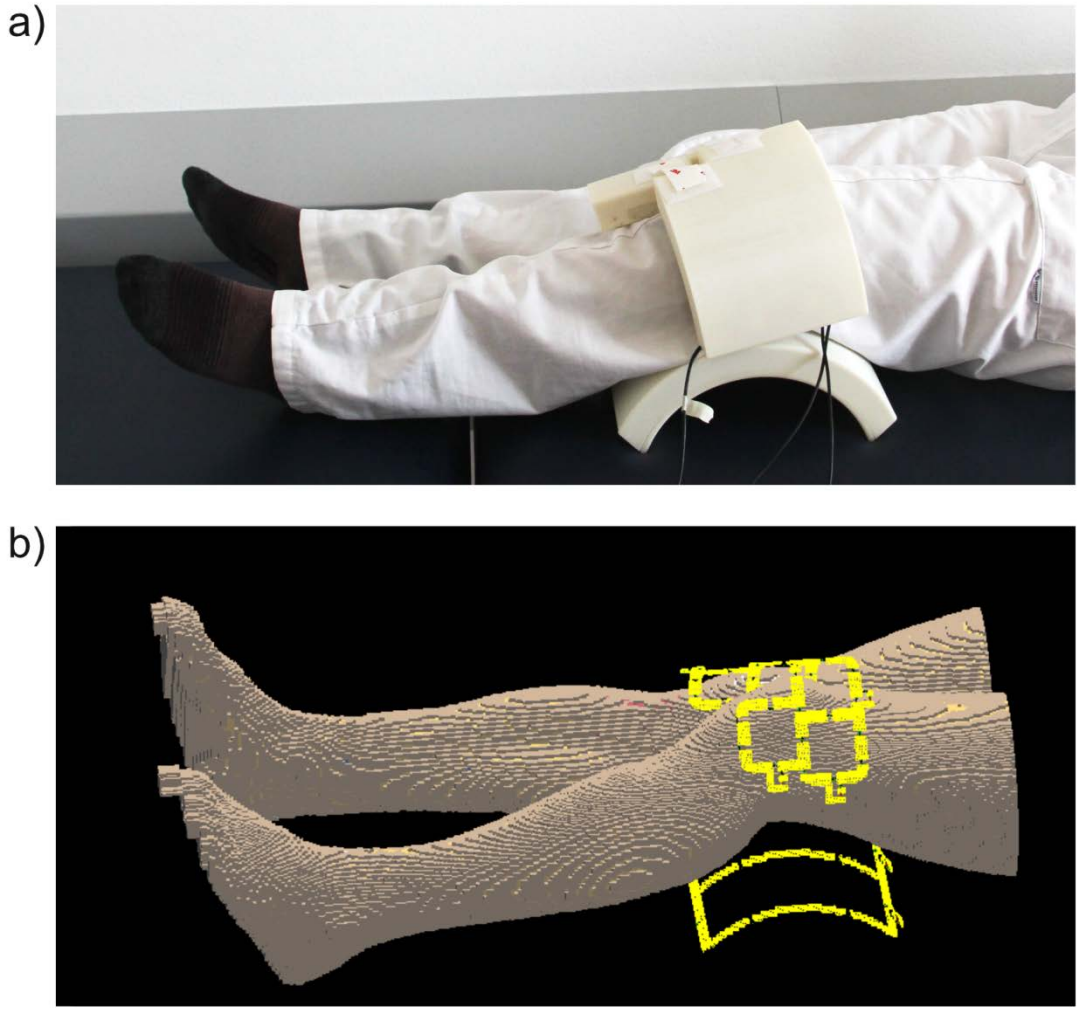

Figure 2

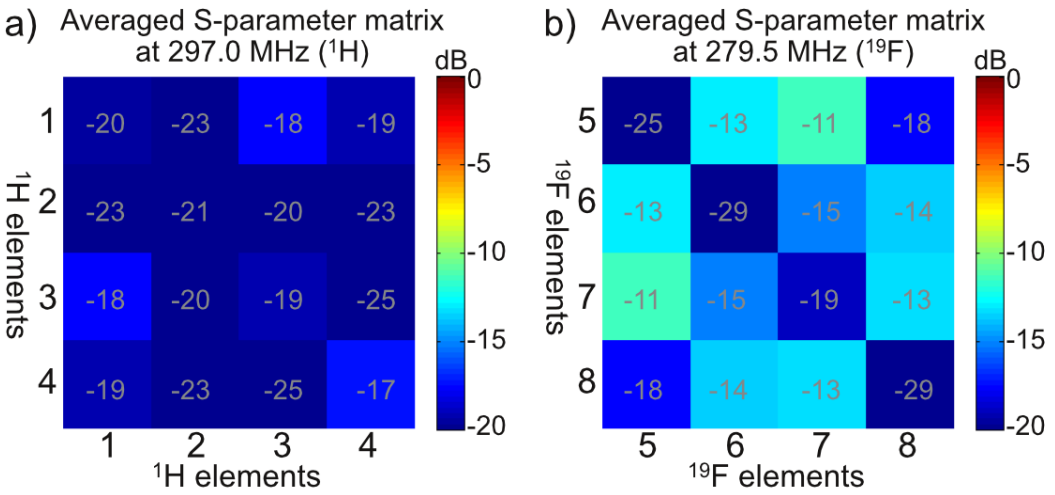

Figure 3

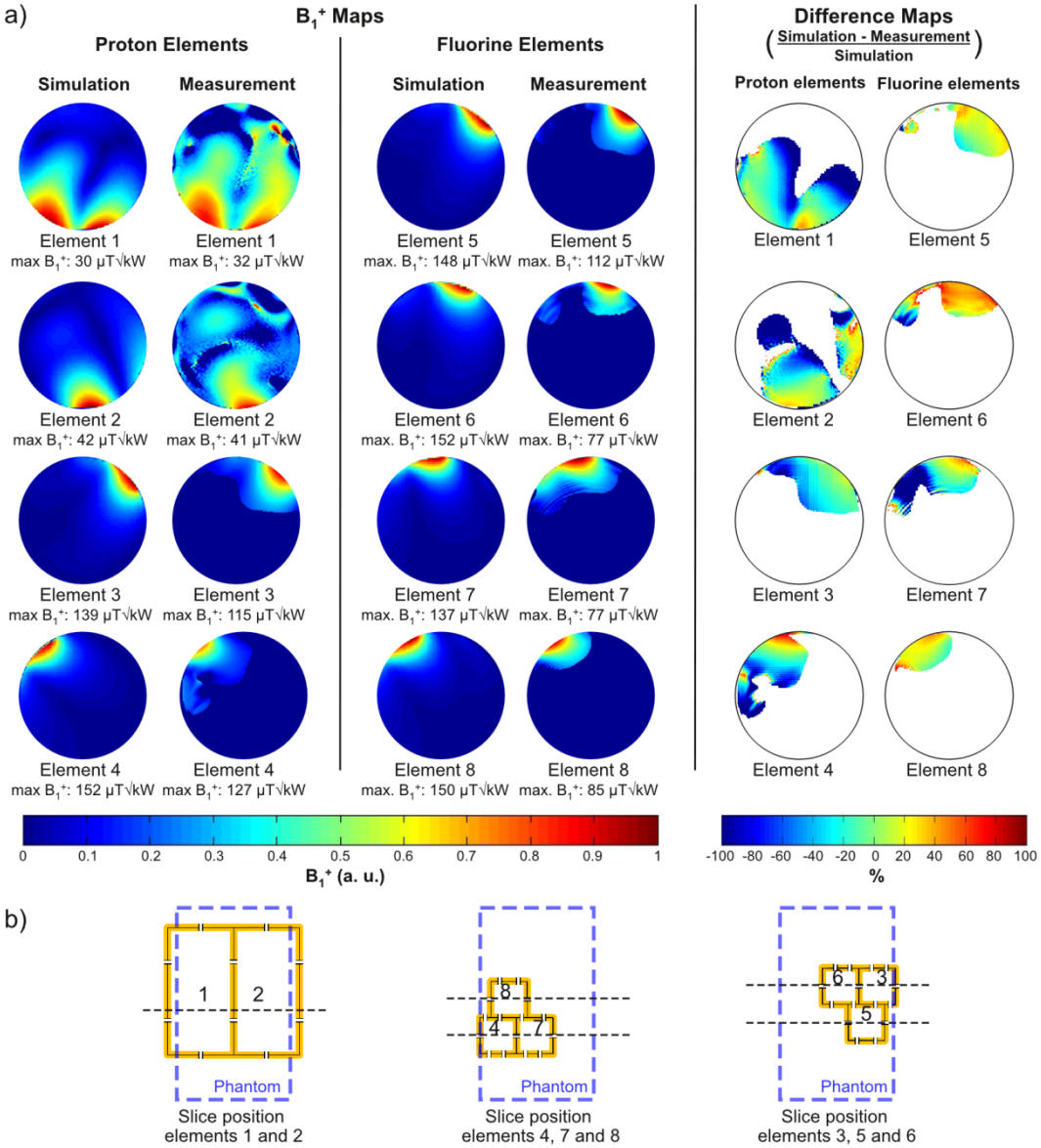

Figure 4

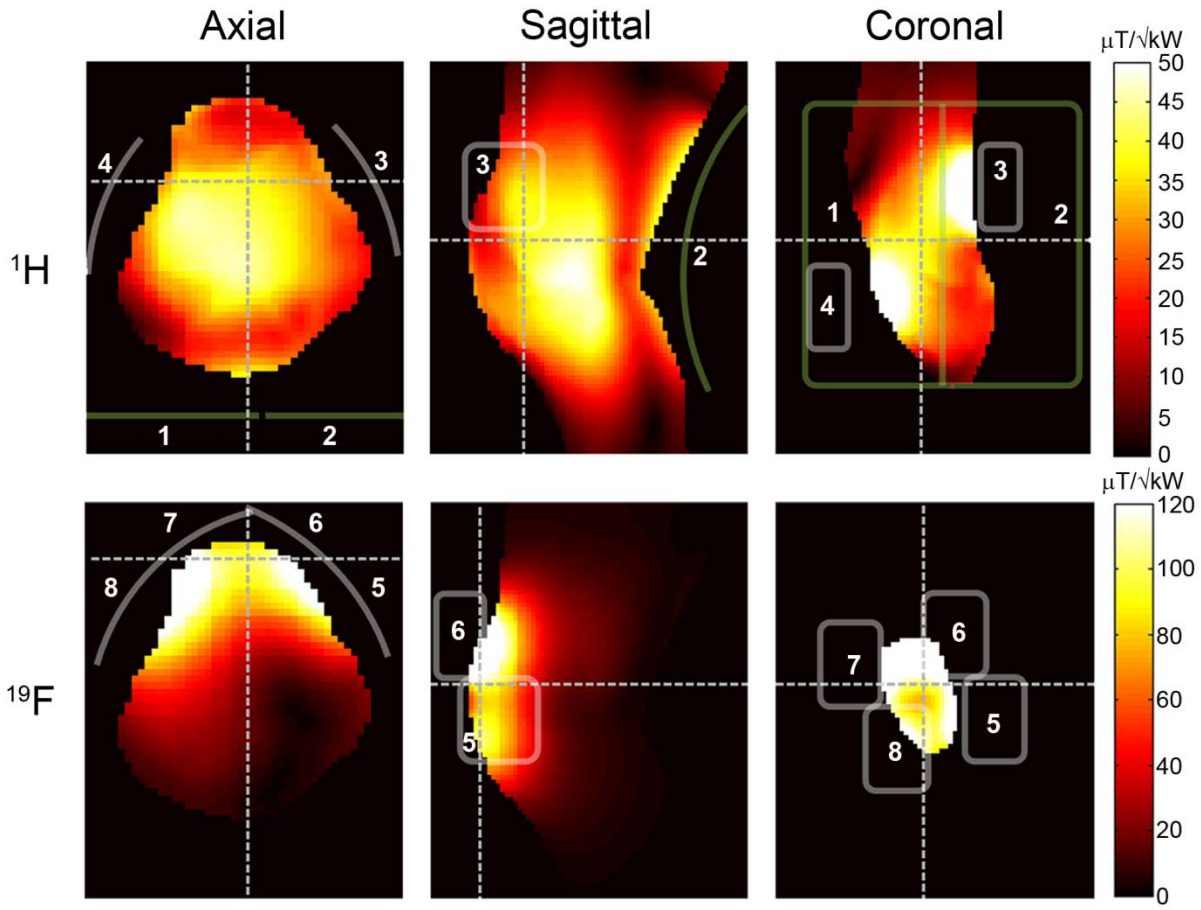
Axial
Sagittal
Coronal
μT/√kW
50
45
40
35
30
25
20
15
10
5
0
^{1}H
4
3
1
2
3
2
1
3
2
4
μT/√kW
120
100
80
60
40
20
0
^{19}F
7
6
8
5
6
5
6
7
5
8

Figure 5

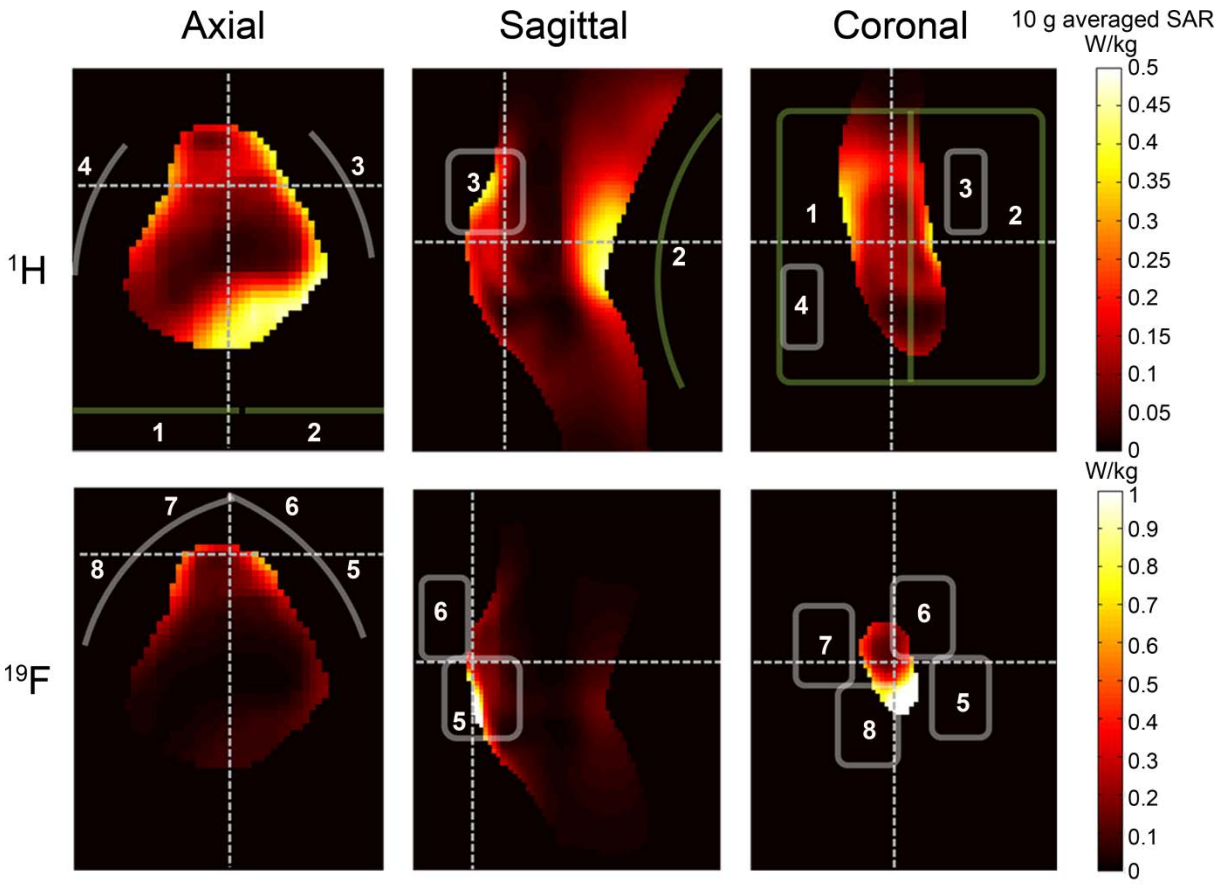
Axial
Sagittal
Coronal
10 g averaged SAR
W/kg
0.5
0.45
0.4
0.35
0.3
0.25
0.2
0.15
0.1
0.05
0
^{1}H
^{19}F
W/kg
1
0.9
0.8
0.7
0.6
0.5
0.4
0.3
0.2
0.1
0

Figure 6

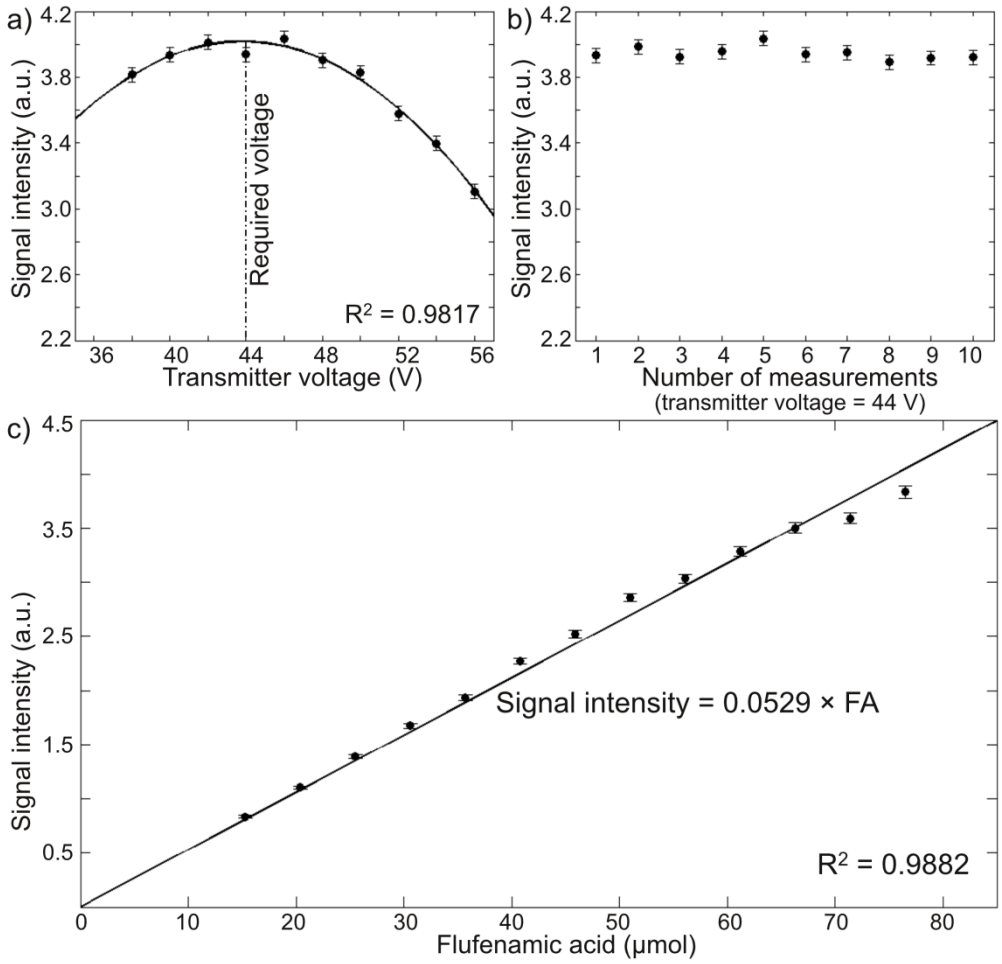

Figure 7

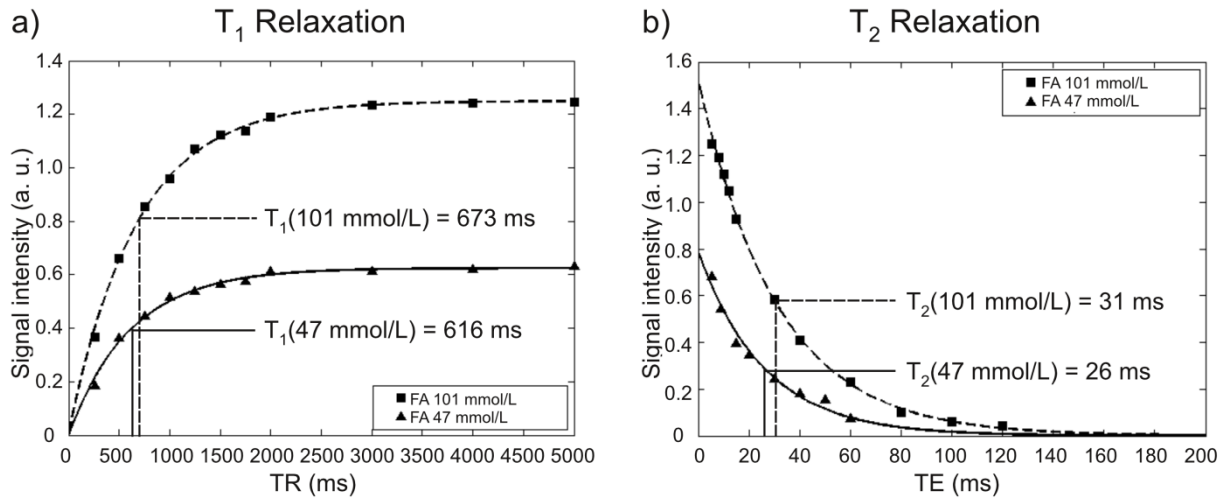

Figure 8

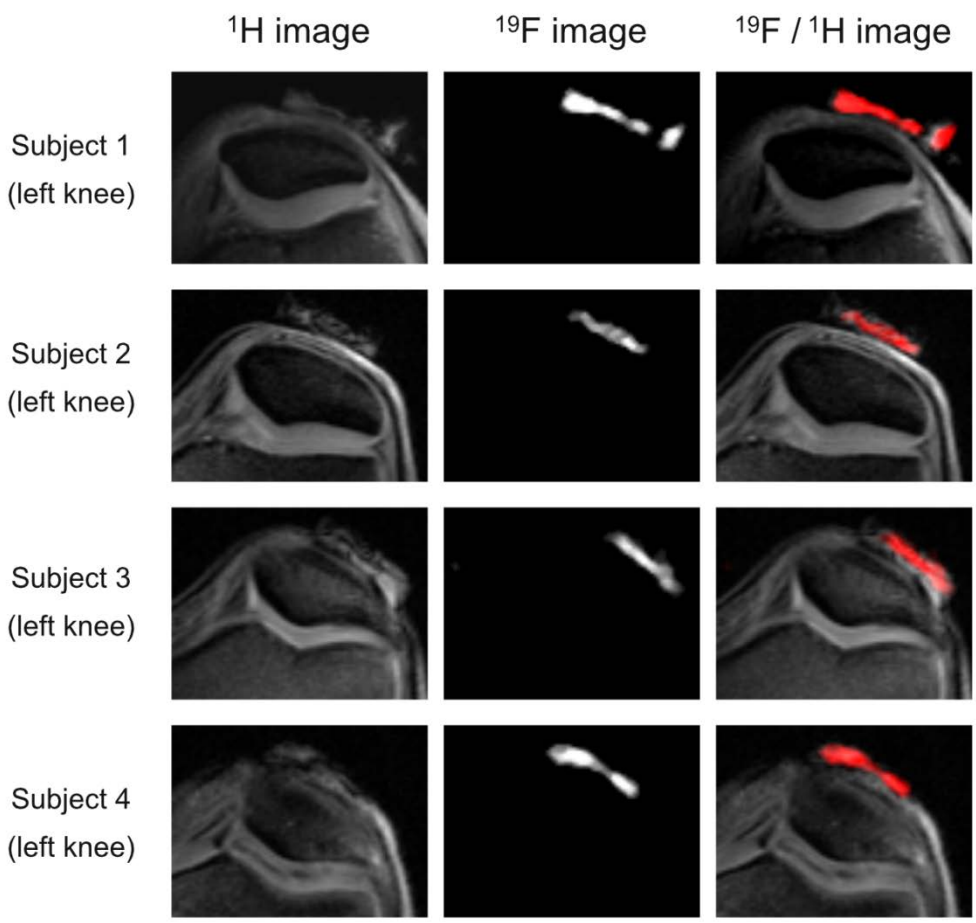
^{1}H image
^{19}F image
^{19}F / ^{1}H image
Subject 1
(left knee)
Subject 2
(left knee)
Subject 3
(left knee)
Subject 4
(left knee)

Figure 9